

Polymorphism in $\text{Cu}_2\text{ZnSnS}_4$ and new off-stoichiometric crystal structure types

Christopher J. Bosson¹, Max T. Birch¹, Douglas P. Halliday^{1*}, Chiu C. Tang², Annette K. Kleppe², Peter D. Hatton¹

¹ Department of Physics, The University of Durham, South Road, Durham, DH1 3LE, UK

² Diamond Light Source, Harwell Science and Innovation Campus, Didcot, OX11 0DE, UK

ABSTRACT: $\text{Cu}_2\text{ZnSnS}_4$ (CZTS) is a very promising material for the absorber layer in sustainable thin-film solar cells. Its photovoltaic performance is currently limited by crystal structure disorder, which causes fluctuations in electrostatic potential that decrease open-circuit voltage. The origin of this disorder is still not fully understood. This work investigates five samples of CZTS over a range of compositions, fabricated by solid-state reaction. Their crystal structures are conclusively identified using high-resolution anomalous X-ray diffraction. Three of the samples display two distinct CZTS phases, evident in minute splitting of some diffraction peaks (by $\sim 0.02^\circ$) due to different c/a lattice parameter ratios. These are attributed to different composition types of CZTS, defined by different charge-neutral defect complexes. In addition to such types previously reported, two new types are proposed: G-type, in which $[2\text{Cu}_{\text{Sn}^{3+}} + \text{Cu}_{\text{Zn}} + \text{Cu}_i + 3\text{V}_{\text{S}^{2+}}]$ defects are prevalent, and H-type, in which $[3\text{S}_i^{2-} + \text{V}_{\text{Cu}} + \text{Zn}_{\text{Cu}} + 2\text{Sn}_{\text{Cu}^{3+}}]$ defects are prevalent. In both cases, the defects probably do not form a single complex due to their large number. Above the order-disorder phase transition the two CZTS phases generally converge to a single phase. A mechanism of phase formation in CZTS is thus proposed. This is the first time CZTS crystal structures have been investigated with sufficiently high resolution to distinguish these different CZTS phases, thereby establishing polymorphic behavior in CZTS.

1. Introduction

In 2016, solar photovoltaic power reached 307 GW peak global capacity, nearly 2 % of global electricity demand.¹ This is growing exponentially as solar takes its place as an important contributor to the energy mix of the future. By 2050, it is predicted that it will contribute 16 % of global electricity use.² However, many materials currently used as the absorber layer of photovoltaic solar cells are problematic. The relatively high manufacturing costs of silicon and material costs of Ga, In, and Te are restrictive for some photovoltaic technologies. Element abundance will limit the capacity of materials containing Te, Se, and In. Toxicity is often another problem, particularly with Cd and Se. Some materials suffer from more than one of these problems.³

$\text{Cu}_2\text{ZnSnS}_4$ (CZTS), however, has none of these problems. It is a semiconductor with a direct band gap of 1.4–1.5 eV, close to the optimal value for photovoltaic performance, has a high band-edge absorption coefficient $>10^4 \text{ cm}^{-1}$, and features intrinsic p-type doping. Its record photovoltaic efficiency is 11.0 %, ⁴ or 12.6 % as the selenium-containing form CZTSSe, which has the disadvantages that selenium is toxic, more expensive, and less abundant than sulphur.⁵ These efficiencies are low compared to the records for silicon (26.6 %⁶), $\text{CuIn}_{1-x}\text{Ga}_x\text{Se}_2$ (CIGS, 22.6 %⁷) and CdTe (22.1 %⁴).

The efficiency of CZTS must be drastically increased for it to be adopted commercially and to enable it to make a large and sustainable contribution to global photovoltaic energy generation on the terawatt scale. For this to happen, the large open-circuit voltage deficit usual for CZTS devices must be decreased from its current typical value of around 40 % of the theoretically possible open-circuit voltage.⁸ The limiting factor in this is likely to be fluctuations in electrostatic potential caused by point defects with relatively deep energy levels, like the antisites Cu_{Zn} and Zn_{Cu} .^{9,10} Additionally, the phase diagram of CZTS is complex and features only a small region in which phase-pure CZTS is stable. The phase diagram has not yet been characterized correctly, and the details of disorder in the crystal structure of CZTS itself have not been fully resolved either. Hence a better understanding of secondary phases and point defects in the CZTS crystal structure is needed to analyze the effect they have on photovoltaic performance.

This work aims to improve the structural understanding of CZTS by performing high-resolution non-resonant and anomalous X-ray powder diffraction experiments on samples over a range of compositions, with full Rietveld refinement considering secondary phases and point defects on all cation lattice sites, using accurate experimentally measured compositions. It follows a neutron diffraction study on two of the same samples that characterized

the order-disorder and kesterite-sphalerite phase transitions CZTS undergoes around 500 K and 1250 K respectively.¹¹

2. CZTS Crystal Structure

CZTS under usual photovoltaic device operating conditions has been calculated to be most stable in the kesterite ($I\bar{4}2m$) crystal structure.¹²⁻¹⁴ Experiments have conclusively confirmed this as the structure adopted, with various degrees of disorder.^{11, 15-19}

This disorder means a high density of antisite defects, primarily only involving copper and zinc due to the very low formation energies of Cu_{Zn} and Zn_{Cu} and the large chemical and size mismatch between tin and the other two cations.²⁰⁻²²

Early descriptions of the disordered kesterite ($I\bar{4}2m$) model had full copper occupancy remaining in the $z = 0$ plane of the kesterite structure (the $2a$ Wyckoff position), with the copper and zinc atoms mixed only in the $z = 1/4$ and $3/4$ planes (the $2c$ and $2d$ Wyckoff positions). However, zinc has been found to substitute for copper at the $2a$ site as the $\text{Cu}/(\text{Zn}+\text{Sn})$ ratio decreases,¹⁵ and recently the $2a$ site has been shown to be equally or more disordered than the $2c$ and $2d$ sites.¹¹ Additionally, copper vacancies have also been reported on the $2a$ site.²³ This means that a fully disordered model with mixing on all Cu and Zn sites is more accurate. The kesterite structure and both of these model disordered structures, referred to as half-disordered and fully disordered respectively, are all depicted in Figure 1.

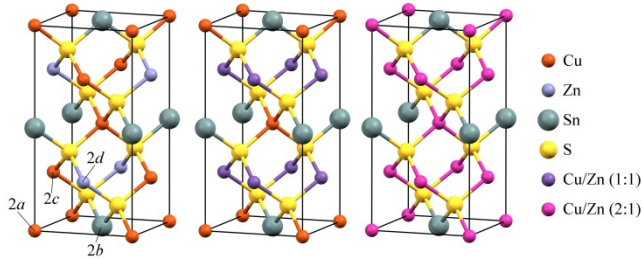


Figure 1. The kesterite (left), half-disordered kesterite (middle), and fully-disordered kesterite (right) crystal structures of CZTS.

Cu_{Zn} and Zn_{Cu} point defects introduce antisite defect energy levels in the band gap (Cu_{Zn} at 0.15 eV above the valence band edge and Zn_{Cu} at 0.10 eV below the conduction band edge²⁴), which act as recombination centers, reducing device efficiency. The Cu_{Zn} defect is the cause of the p-type behavior in stoichiometric CZTS, but it is replaced as the dominant acceptor by the copper vacancy (V_{Cu}) for Cu poor, Zn rich compositions, which have been found to give the best device efficiencies.²⁵

In addition to individual point defects, several charge compensating defect complexes have been calculated to form in CZTS. They lower the formation energies of the defects involved due to the electrostatic attraction be-

tween them. $[\text{Cu}_{\text{Zn}}^- + \text{Zn}_{\text{Cu}}^+]$ and $[\text{V}_{\text{Cu}}^- + \text{Zn}_{\text{Cu}}^+]$ complexes have been found to be the most common.²⁴

Several of these stable defect complexes have been observed to form long-range order in CZTS to the extent that they are responsible for grains of discrete CZTS phases, with particular stoichiometries.²⁶⁻²⁸ These are described in Table 1. The stoichiometries that can be formed by incorporation of these defect complexes are plotted in Figure 2. The stability provided by these off-stoichiometric defect complexes extends the region of stability of single-phase CZTS beyond that calculated as very small in the usual ternary phase diagram.²⁹

CZTS type	Defect complex	Stoichiometry
S-type	$[\text{Cu}_{\text{Zn}}^- + \text{Zn}_{\text{Cu}}^+]$	Stoichiometric
A-type	$[\text{V}_{\text{Cu}}^- + \text{Zn}_{\text{Cu}}^+]$	Cu-poor, Zn-rich
B-type	$[\text{Zn}_{\text{Sn}^{2-}} + 2\text{Zn}_{\text{Cu}}^+]$	Cu-poor, Zn-rich
C-type	$[2\text{Cu}_{\text{Zn}}^- + \text{Sn}_{\text{Zn}^{2+}}]$	Cu-rich, Zn-poor
D-type	$[\text{Cu}_{\text{Zn}}^- + \text{Cu}_i^+]$	Cu-rich, Zn-poor
E-type	$[2\text{V}_{\text{Cu}}^- + \text{Sn}_{\text{Zn}^{2+}}]/[\text{V}_{\text{Zn}^{2-}} + \text{V}_{\text{Cu}}^- + \text{Sn}_{\text{Cu}^{3+}}]$	Cu-poor, Sn-rich
F-type	$[\text{Zn}_{\text{Sn}^{2-}} + 2\text{Cu}_i^+]/[\text{Cu}_{\text{Sn}^{3-}} + \text{Zn}_i^{2+} + \text{Cu}_i^+]$	Cu-rich, Sn-poor

Table 1. The types of CZTS as defined by Lafond et al.,²⁶ Gurieva et al.,²⁷ and Valle-Rios et al.,²⁸ with an additional entry for stoichiometric, or S-type, CZTS.

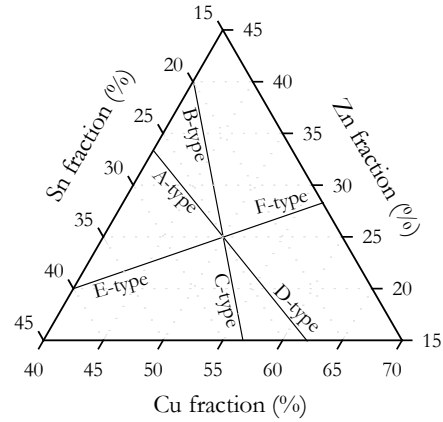


Figure 2. The compositions of the defect-complex-defined types of CZTS. S-type lies only on the stoichiometric point at the center and the other types lie along the labelled lines, with the exact location along the line determined by the number density of the respective defect complex.²⁶⁻²⁸

A second-order phase transition from the nominally ordered to a nominally disordered kesterite structure has been identified between 489 K and 552 K, with the exact transition temperature dependent on the stoichiometry of the CZTS.^{11, 30-32} Usual device synthesis conditions involve a sulphurisation annealing stage above this transition temperature, so a disordered structure is initially formed. Only during the cooling process below the critical temperature can ordering then occur. Hence, the disorder can in principal be controlled using the cooling process. It has

previously been reported that 50 % antisite population at the 2c and 2d sites in water-quenched samples was reduced to 30 % in samples with a controlled cooling rate.¹⁶

The ability to resolve the exact disorder in the crystal structure of CZTS samples is of significant importance, but it is not possible to do so using conventional powder X-ray diffraction (XRD), which is normally used for such identification in other materials. This is because copper and zinc are isoelectronic in CZTS, as Cu^+ and Zn^{2+} ions, meaning their X-ray scattering form factors are the same, because they are proportional to atomic number Z . This can be overcome by using anomalous X-ray diffraction.

Anomalous scattering is the variation in atomic scattering factor for energies close to an absorption edge. It is accounted for by a correction of the form $f = f_o + f' + i f''$, where f_o is the uncorrected scattering factor, f' is the change in scattering factor magnitude and f'' is a phase shift. By comparing a non-resonant spectrum with one just below an absorption edge, where f' is large, scattering due to the respective element can be highlighted.

Secondary phases are also often present in samples of CZTS because the stability region of pure CZTS in the composition phase diagram is small.^{33, 34} ZnS , which forms a barrier to carrier extraction due to its large band gap, and Cu_2SnS_3 , which acts as a recombination center and reduces the open-circuit voltage, are the most common. CuS , Cu_2S , SnS , SnS_2 , Sn_2S_3 , Cu_3SnS_4 , Cu_4SnS_4 , $\text{Cu}_4\text{Sn}_7\text{S}_{16}$, and $\text{Cu}_2\text{ZnSn}_3\text{S}_8$ can also be present.³⁵ Detecting the most common secondary phases using conventional powder diffraction is not usually possible, because the diffraction peaks overlap those of CZTS within the resolution of standard equipment.³⁶

The high resolution offered by synchrotron XRD coupled with the unique ability of anomalous scattering to distinguish copper and zinc ions overcome these issues, and can allow the accurate identification of all phases in CZTS samples as well as defects within the CZTS structure.

3. Experimental Details

Bulk polycrystalline samples were fabricated by solid-state reaction. Fine-grained powders of copper, zinc, and tin (with purities of 99.9 %, 97.5 %, and 99.85 % respectively) were well mixed and placed in one alumina boat and sulphur powder was placed in a second boat (99.5 % pure, with a 30 % excess for full sulphurisation). The boats were sealed together in a quartz ampoule under vacuum. The ampoules were heated in a tube furnace to 1073 K with a ramping rate of $5 \text{ K}\cdot\text{min}^{-1}$, kept at that temperature for 24 hours, and then left to cool naturally in the furnace over around 24 hours. Samples were produced with five different compositions. The sample ingots were ground to a fine powder using an agate mortar for diffraction experiments.

The elemental compositions of the samples post-fabrication was measured using inductively coupled plasma mass spectroscopy (ICPMS) carried out with an Elan 6000 Perkin Elmer Sciex ICPMS. SEM images were

taken using an Hitachi SU-70 FEG SEM. The same SEM, with an INCA x-act LN₂-free analytical silicon drift detector and INCA software, was used for EDX spectroscopy. A Bruker Avance III HD spectrometer was used to take ⁶⁵Cu solid state nuclear magnetic resonance (SSNMR) measurements. Spectra were referenced to samples of $[\text{Cu}(\text{CH}_3\text{CN})_4][\text{PF}_6]$ saturated in MeCN. A Horiba JY LabRAM-HR Raman microscope system was used to record Raman spectra in the backscattering configuration with CZTS-resonant excitation at 785 nm provided by an LED laser.

Anomalous powder X-ray diffraction experiments were carried out at Diamond Light Source. The I15 beamline was used for the Sn K absorption edge at 29.2 keV (samples B21 and B22 only), and the I11 beamline^[37] for the Cu and Zn K absorption edges at 8.98 and 9.66 keV respectively. For the Sn edge, resonant patterns were taken precisely at the edge and comparative non-resonant patterns were taken 2 keV below it. For the Cu and Zn edges, resonant patterns were taken 10 eV below each edge and comparative non-resonant patterns at 15 keV, both at 300 K and 600 K. The Cu and Zn absorption edges were calibrated from the fluorescence signals of the samples by scanning the monochromator. Rietveld refinement was carried out using TOPAS v6. Resonant and non-resonant data files were modelled simultaneously, including multiple phases, the elemental composition of CZTS phases, disorder on all CZTS cation sites, and vacancies on all CZTS sites.

4. Results and Analysis

4.1. Composition

The post-fabrication cation compositions are plotted in Figure 3 relative to the defect complex defined off-stoichiometric type compositions.

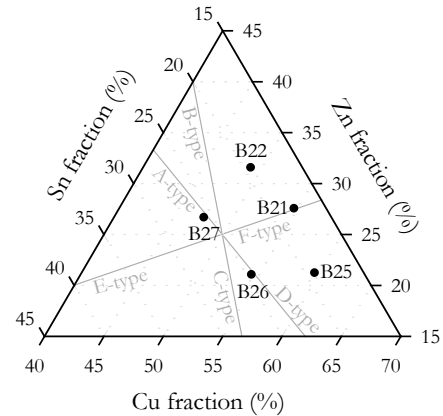


Figure 3. The compositions of the samples measured by ICPMS, shown with the compositions of the defect-complex-defined off-stoichiometric CZTS types.

4.2. Morphology and Secondary Phases

SEM images of the samples are given in Figure 4, showing that they are very porous. EDX identified no second-

ary phases in B21 or B25, only negligible amounts of ZnS and SnS₂ in B22, and Cu₄Sn₇S₁₆ in both B26 and B27.

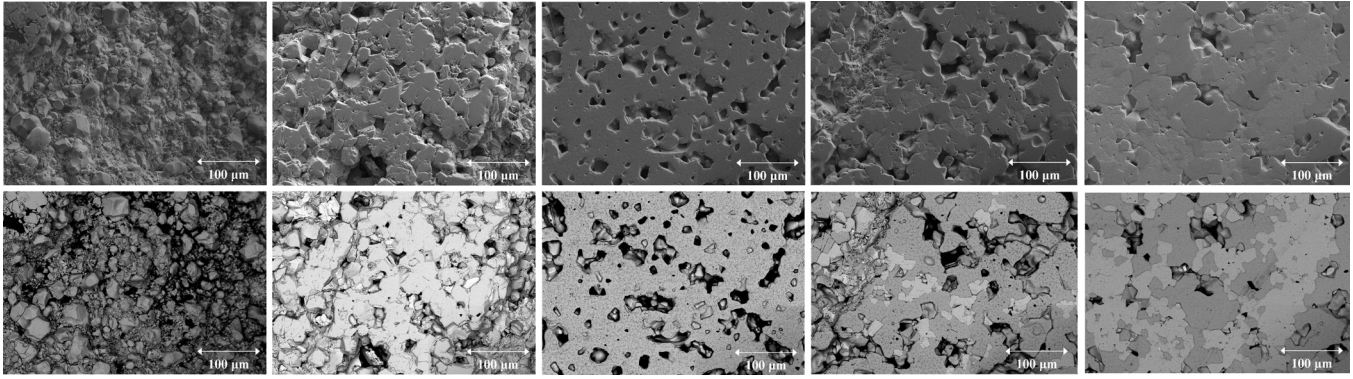


Figure 4. SEM images (top, secondary electron; and bottom, backscattered) of (left to right) B21, B22, B25, B26, & B27.

The SSNMR spectra, shown in Figure 5, confirm that the majority of all samples is kesterite CZTS. The band-shapes of samples B21 and B22 both exactly match those in the literature for pure CZTS.³⁸ The small peak at 280 ppm for B26 and B27 corresponds to the Cu₄Sn₇S₁₆ phase. The peaks for B25 and B26 are so broad that the distinct shifts due to the 2a and 2c lattice sites cannot be distinguished, suggesting either extreme disorder within the kesterite structure or a secondary phase with copper in similar chemical environments, such as Cu₃SnS₄.

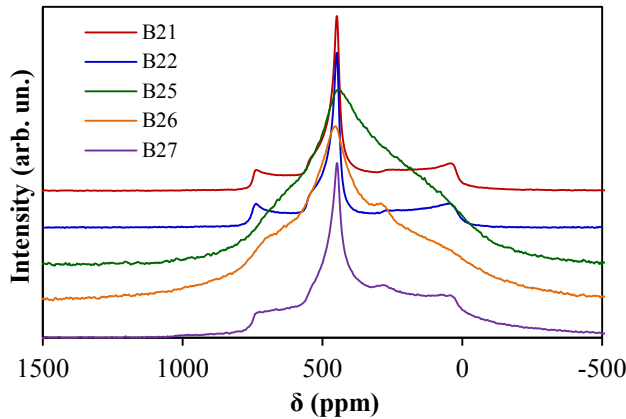


Figure 5: ⁶⁵Cu SSNMR spectra.

The Raman spectra, shown in Figure 6, were modelled using up to 12 peaks previously reported and identified in the literature.³⁹⁻⁴⁵ They also confirm the majority presence of CZTS in all samples, with a significant Cu₃SnS₄ presence in B26 (and much smaller amount in B21) shown by the peak at 318 cm⁻¹, and a particularly large amount of disorder in B25 shown by the main CZTS peak being shifted to lower wavenumber. The very broad NMR peaks for B25 and B26 thus have different causes despite appearing very similar: simple disorder in B25 and Cu₃SnS₄ in B26. The Cu₃SnS₄ in B26 was not identified by EDX because that technique is not sensitive to the difference between copper and zinc, so it cannot accurately distinguish between CZTS and Cu₃SnS₄.

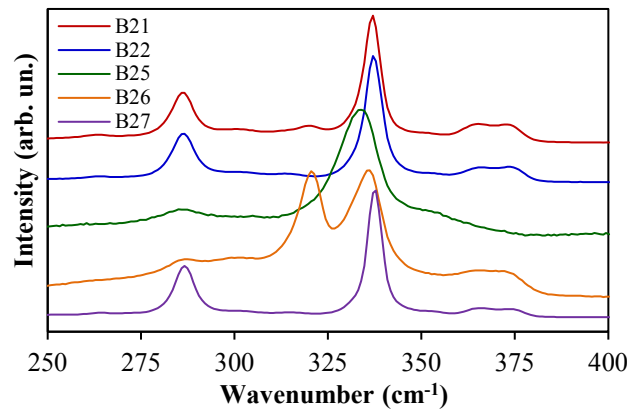


Figure 6. Normalised Raman spectra taken using resonant 785 nm excitation.

The secondary phases concluded to be present in each sample from combining the EDX, NMR, and Raman results are given in Table 2. CZTS is known to have a very small region of stability around the stoichiometric composition, so it is unsurprising that secondary phases are found in most samples.

Sample	Secondary phases
B21	(negligible Cu ₃ SnS ₄)
B22	(negligible ZnS and SnS ₂)
B25	(None)
B26	Cu ₃ SnS ₄ , Cu ₄ Sn ₇ S ₁₆
B27	Cu ₄ Sn ₇ S ₁₆

Table 2. The secondary phases identified in each sample in addition to CZTS from combining EDX, NMR, and Raman results. Additionally B25 contains very high Cu-Zn disorder in the CZTS.

4.3. Diffraction Results

Due to the high resolution of the I11 beamline at Diamond and good sample crystallinity, the crystal structures

of the samples can be determined with the highest accuracy and precision to date. Typical non-resonant X-ray diffraction patterns from I15 and I11 are shown in Figure 7 and Figure 8 respectively.

Refinement using the Sn-edge X-ray data for B21 and B22 showed no disorder involving tin, as expected – it is all found on the $2b$ site. Interpretation of the Cu and Zn edge patterns is more complicated.

4.3.1. Phases Present at 300 K

Identifying the phases to include in refinements of the I11 patterns was not straightforward. The 300 K patterns of B21, B25, B26, & B27 exhibit small peak splitting ($\Delta 2\theta \sim 0.02^\circ$) for some peaks of the CZTS pattern, pictured in the inset of Figure 8, and in Figure 9. This is the first report of diffraction at such high resolution on CZTS, meaning this is the first time such small splitting has been observed.

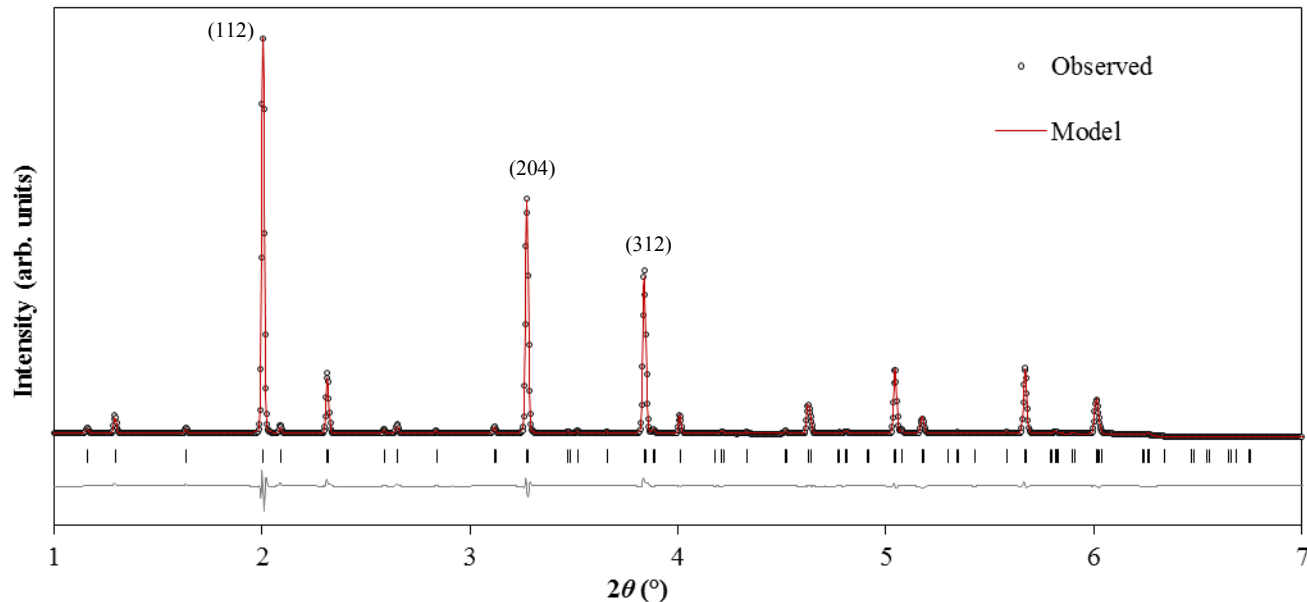


Figure 7. X-ray diffraction pattern for B21 taken at room temperature using 27.2 keV X-rays at Diamond I15, showing a kesterite best-fit model plotted over the data, with the peak positions marked below the pattern, and the residual at the bottom.

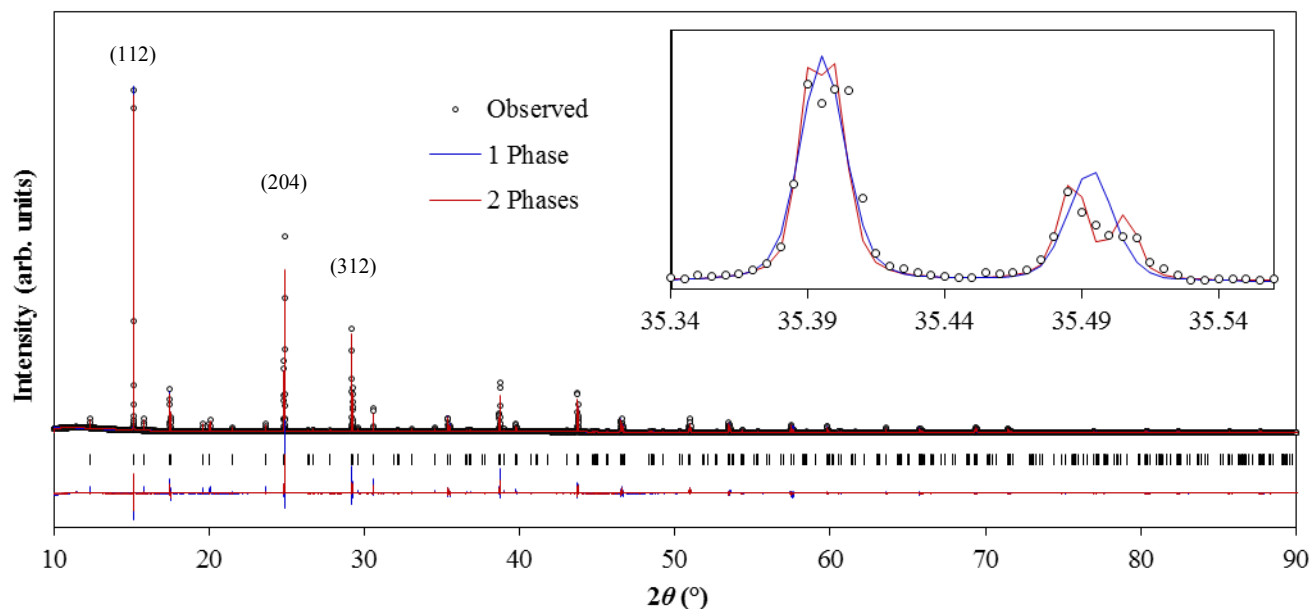


Figure 8. X-ray diffraction pattern for B21 taken at room temperature using 15 keV X-rays at Diamond I11, showing models with a single kesterite phase and with two kesterite phases plotted over the data, the peak positions marked below the patterns, and the residuals for each model at the bottom. Inset are the (400) and (008) peaks, showing peak splitting by $\sim 0.1^\circ$ due to the tetragonal ratio $a/2c$ being slightly less than one, and each individual peak showing further slight splitting of $\sim 0.02^\circ$ due to two nearly identical tetragonal phases being present.

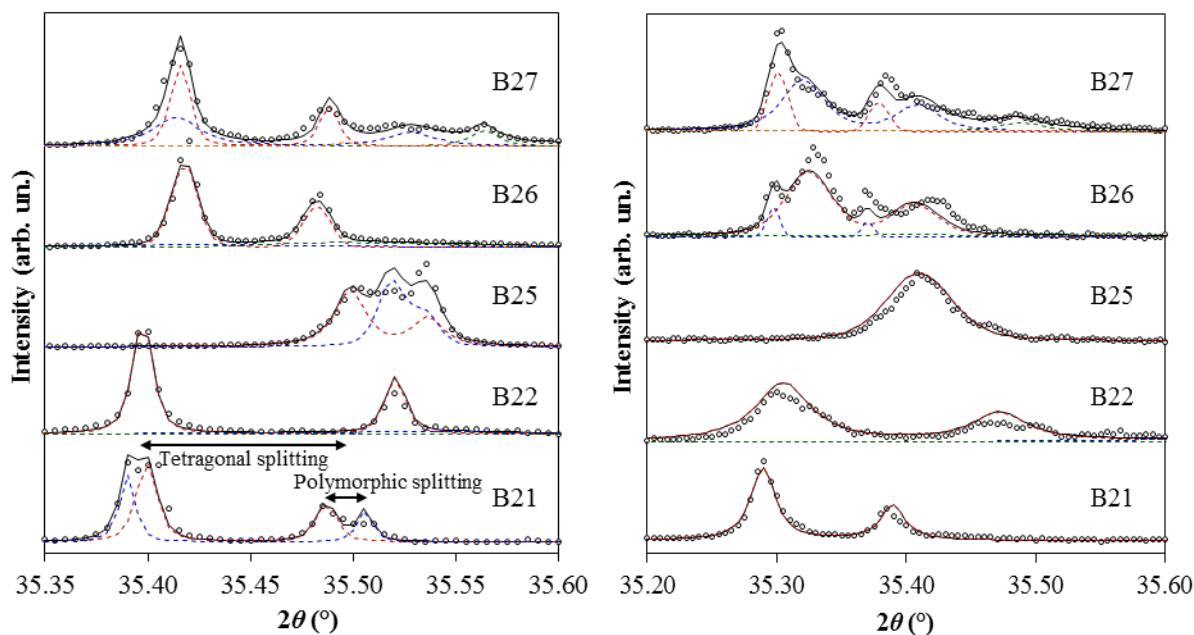


Figure 9. Peak splitting due to multiple phases in the 15 keV patterns; left, at 300 K; and right at 600 K. The circles show the experimental data, the solid black line the total model intensity, and the dashed lines the contribution of each individual phase to the model.

Pawley refinements revealed that these phases are all tetragonal, ruling out the cubic ZnS secondary phase. The possible explanations for the multiple structures are therefore: a similar tetragonal secondary phase (Cu_2SnS_3 or Cu_3SnS_4 ; N.B. Cu_4SnS_4 has a significantly different structure and hence diffraction pattern), or two CZTS structures with slightly different lattice parameters, which could be both kesterite, both stannite, or one of each.

For all samples, a two-stannite-phases model and a kesterite-and-stannite model are both ruled out because they give a poorer fit to the data than the other options: the stannite structure does not contribute intensity to several peaks, such as (123) and (231).

For B21, Cu_2SnS_3 and Cu_3SnS_4 are discounted because they give a poor fit to the data, particularly the low-intensity peaks, and because the NMR and Raman results showed no significant sign of these materials. A mixture of two kesterite CZTS phases is therefore the best model.

For B22, the CZTS peaks do not exhibit the very small peak-splitting with $\Delta 2\theta \sim 0.02^\circ$. The patterns include distinct ZnS and SnS_2 peaks consistent with these phases having been identified by EDX.

For B25, the tetragonal splitting is much less than the other samples, which could be a result of the significant disorder indicated in the NMR and Raman spectra. Cu_3SnS_4 is ruled out as the second tetragonal phase because it is not evident in the Raman spectrum, but Cu_2SnS_3 is a possibility. However, as for B21, two kesterite CZTS phases gives a slightly better fit to the data, so this is adopted as the best-fit model.

For B26, Raman measurements show that Cu_3SnS_4 makes up a significant fraction of the sample, and so the

second tetragonal structure evident in the diffraction patterns for B26 is assigned as Cu_3SnS_4 rather than a second CZTS phase or Cu_2SnS_3 . The $\text{Cu}_4\text{Sn}_7\text{S}_{16}$ identified by EDX and NMR is clearly evident in the diffraction patterns too.

For B27, which has the most complicated collection of peaks in its diffraction patterns, small amounts of ZnS and Cu_2SnS_3 were clearly identified in addition to the $\text{Cu}_4\text{Sn}_7\text{S}_{16}$ identified by EDX and NMR. They are present in quantities small enough not to have been identified by the other techniques. A second CZTS pattern is observed for this sample too. Cu_3SnS_4 is ruled out because it was not observed using Raman analysis.

Despite the high-resolution of the data, the presence of secondary phases and the overlapping of peaks make the assignment of phases using the diffraction data to some degree subjective – particularly for B27. The structural models presented in this paper are consistent with all results, but may not be the only possible models for some samples. However, the unique ability of anomalous-scattering XRD to resolve copper and zinc gives confidence in the accuracy of differences in refinements using CZTS, Cu_2SnS_3 , and Cu_3SnS_4 , meaning these phases can be distinguished with a high degree of confidence.

The best-fit models of the sample phase compositions are given in Table 3. In all the CZTS structures, significant mixing of copper and zinc on the cation sites was observed, which will be discussed below.

Sample	CZTS Phases		Secondary Phases		
B21	B-type 56 %	G-type 44 %			
B22	F-type 84 %		SnS ₂ 9 %	ZnS 7 %	
B25	G-type 53 %	S-type 47 %			
B26	F-type 71 %		Cu ₄ Sn ₇ S ₁₆ 17 %	Cu ₃ SnS ₄ 12 %	
B27	B-type 38 %	D-type 35 %	Cu ₄ Sn ₇ S ₁₆ 17 %	ZnS 9 %	Cu ₂ SnS ₃ 2 %

Table 3. The phase compositions of all samples at 300 K determined by Rietveld refinement of I11 data.

The two samples that formed Cu₄Sn₇S₁₆ (B26 and B27) are those richest in tin, with approximately stoichiometric tin content, which is to be expected given the high tin content of Cu₄Sn₇S₁₆. A relatively small amount of ZnS was only found in two of the three Zn-rich samples (B22 and B27); it is unclear why none was formed in B21. Interestingly, only a very small amount of Cu₂SnS₃ was formed in only one sample (B27), despite being considered one of the major secondary phases in CZTS. The Cu-rich, Zn-poor composition of B26 explains the formation of a significant amount of Cu₃SnS₄. It seems that a Sn-poor or significantly Zn-rich composition prevents the formation of ternary secondary phases.

4.3.2. CZTS Phase Types

The composition of each CZTS phase was allowed to vary during refinement, with the weighted average composition of all phases in the sample constrained to the measured overall sample composition. The best-fit compositions of each CZTS phase are plotted in Figure 10.

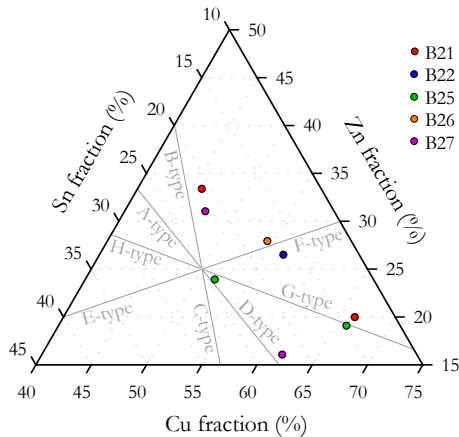


Figure 10. The atomic compositions of each CZTS phase at 300 K, including two new types proposed here: G and H.

All the phase compositions correspond approximately to an established defect-complex-defined CZTS type with the exception of one of the B21 phases and one of the B25 phases, which both have approximately the same composition. Two new composition types, labelled G and H, are therefore proposed based on this composition and its opposite through the stoichiometric point. These are given in Table 4.

CZTS type	Defect complex	Stoichiometry
G-type	[2Cu _{Sn} ³⁺ + Cu _{Zn} ⁻ + Cu _i ⁺ + 3V _S ²⁺]	Sn-poor, Cu-rich
H-type	[3S _i ²⁻ + V _{Cu} ⁻ + Zn _{Cu} ⁺ + 2Sn _{Cu} ³⁺]	Cu-rich, Sn-poor

Table 4. Two proposed new types of CZTS, with composition defined by the prevalence of the respective defects.

The defects required to achieve the compositions of the two new types are greater in number than those of the previously identified types. This draws into question whether they exist as single complexes or are better thought of as smaller complexes occurring in the same grains, for example the G-type defects could be grouped as [Cu_{Sn}³⁺ + Cu_i⁺ + V_S²⁺] and [Cu_{Sn}³⁺ + Cu_{Zn}⁻ + 2V_S²⁺] charge-neutral complexes. The greater number of defects required to explain the compositions may be the reason why these types have not yet been reported.

It is notable that the new types involve sulphur-related defects; G-type is S-poor and H-type is S-rich. The possibility of incomplete sulphurisation during CZTS fabrication has long been established, but this is rarely taken into consideration when predicting or attempting to explain secondary phases, despite its obvious impact.

These results may at last shed some light on the complex mechanism of secondary phase formation in CZTS samples, which has for so long seemed mysterious because the predictions of calculations did not match the secondary phases found by experiments. It is not simply a question of which secondary phases are stable for a given composition, but which combination of type(s) of CZTS and secondary phases is energetically favorable.

Even when a sample has overall composition equal to a CZTS type, a phase-pure sample of that type is not necessarily the most stable. The sample composition of B21 almost exactly fits F-type CZTS, but the sample actually formed a mixture of B-type and G-type. That of B25 matches G-type CZTS, but the samples split into a mixture of S-type and G-type with a higher defect density. The sample composition of B27 matches A-type (or possibly S-type) CZTS, but it split into B-type and D-type.

A theoretical study of the formation energy not just of individual point defect complexes, but of a multi-phase sample as a function of phases present, phase fractions, and defect complex density within the CZTS phase(s) would be enlightening, but perhaps prohibitively computationally demanding.

4.3.3. Cu-Zn Disorder

The lattice site occupancies of each phase of CZTS in the best models from simultaneous Rietveld refinement of resonant and non-resonant patterns are given in Table 5. These can be used to check whether the type-defining defect complexes are in fact responsible for the phase compositions.

It is found that these results largely match the defects of the complexes of the respective CZTS types, where possible. Some additional defects of other kinds are present in small concentrations in most cases, as is to be expected in real rather than ideal samples.

However, it should be noted that interstitial defects were not modelled during this work due to technical limitations. This means that those types predicted to feature significant interstitial presence (D-type, F-type, and G-type), cannot be accurately represented in the site occupancies given in Table 5. For the D-type phase of B27, Zn_{Cu} and Cu_{Sn} are overrepresented; for the 'F-type' phase of B22 and B26, vacancies are overrepresented; for the 'G-type' phase of B21, V_{Cu} and V_{Zn} are overrepresented;

and for the 'G-type' phase of B25, Zn_{Cu} and Zn_{Sn} are overrepresented and Cu_{Sn} underrepresented. In each case this is because interstitials cannot be modelled and so other refinement results with the same composition are returned instead.

Cu-Zn mixing, which does not affect phase stoichiometry, was observed to some extent in most phases in addition to the disorder from defect complexes. These results confirm recent findings that the $2a$ site features Zn_{Cu} occupancy as much as the $2c$ site. The process of ordering is clearly more complicated than a function of annealing time and temperature described by a single, simple order parameter for mixing of two elements on two sites, as has previously been used. Cu-Zn disorder occurs on all four cation sites. Further investigation is clearly required to understand the complexities of this disorder, and to find the optimum procedure to promote cation ordering. It should also be noted that significant sulphur vacancy was observed in all CZTS phases, which has rarely been considered in previous studies of disorder in CZTS.

CZTS type	Sample	$2a$	$2c$	$2d$	$2b$	$8g$	a (Å)	c (Å)
S-type	B25						5.417766(9)	10.83068(3)
	B21						5.433014(6)	10.84009(1)
B-type	B27						5.433021(7)	10.84460(2)
	B27						5.433374(9)	10.83298(4)
D-type	B22						5.433263(4)	10.83005(1)
	B26						5.432676(3)	10.84625(8)
F-type	B21						5.434419(5)	10.83451(1)
	B25						5.420721(9)	10.83023(6)
G-type	B25						5.420721(9)	10.83023(6)

Table 5. The lattice site occupancies (red represents copper, blue zinc, grey tin, and yellow sulphur) and lattice parameters of the modelled CZTS phases at 300 K, grouped by type.

4.3.4. Phase Transition

In the 600 K patterns the same secondary phases were identified in each sample at approximately the same phase fractions as at 300 K. However, as can be seen in Figure 9, the peak splitting due to two CZTS phases disappears between the 300 K and 600 K patterns for samples B21 and B25, but persists in B27. The peak splitting becomes more pronounced in B26, but as the second peaks are due to Cu_3SnS_4 rather than a second CZTS phase this is unsurprising. The compositions of the remaining CZTS phases at 600 K are plotted in Figure 11.

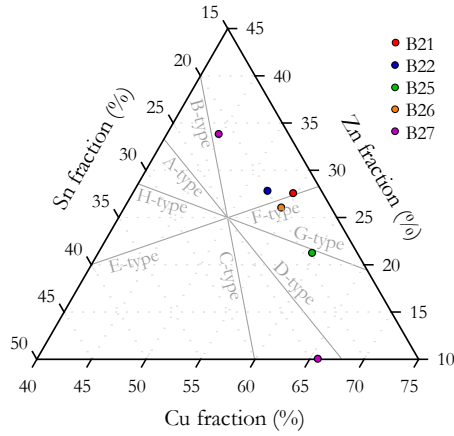


Figure 11. The atomic compositions of each CZTS phase at 600 K.

This phase convergence implies that above the order-disorder transition a single CZTS phase is generally energetically favorable over two separate phases. That the two CZTS phases persist in B27 could suggest that the transition temperature may be above 600 K for that composition or for one of those CZTS types. However, the lattice site occupancies, depicted in Table 6, show that the B27 CZTS phases are also more disordered at 600 K than at 300 K, showing that the transition has in fact taken place. Two CZTS phases are simply still energetically favorable above it in the specific case of the composition of B27.

For the samples with only a single phase of CZTS (B22 and B26) the composition of the CZTS phase remains of the same type, which is unsurprising as the temperature is not high enough to change the secondary phase fractions. In B27, both CZTS phases retain their types, but feature more of the respective defects (i.e. move outwards from the stoichiometric point). For the samples for which two CZTS phases converge (B21 and B25), the composition of the high-temperature phase is simply a weighted average of the two 300 K phases, and is additionally of an off-stoichiometric defect-complex-defined type itself: F-type for B21 and G-type for B25.

CZTS type	Sample	2a	2c	2d	2b	8g	a (Å)	c (Å)
B-type	B27						5.44737(6)	10.8683(1)
D-type	B27						5.45024(4)	10.87726(9)
	B21						5.44913(4)	10.86843(8)
F-type	B22						5.44759(6)	10.8656(1)
	B26						5.44738(5)	10.8704(1)
G-type	B25						5.43468(5)	10.8641(1)

Table 6. The lattice site occupancies (red represents copper, blue zinc, grey tin, and yellow sulphur) and lattice parameters of the modelled CZTS phases at 600 K, grouped by type.

This illuminates the formation mechanism of the CZTS phases. During the cooling process of sample fabrication a single CZTS phase is generally, but not always, formed first, defined by the stability of the combination of that CZTS composition and any secondary phases. This CZTS phase then splits into separate grains of two different type phases as the sample cools below the transition temperature, if such a mixture is energetically favorable over the single phase.

It is possible that this convergence/splitting of CZTS phases is actually what has been previously observed and identified as an ‘order-disorder’ transition. However, the 600 K lattice site occupancies of the CZTS phases, illustrated in Table 6, show much greater Cu-Zn disorder than the 300 K structures, approximating the fully disordered kesterite structure within the bounds of the type compositions. Hence an order-disorder transition can still be seen to take place, in addition to the convergence of the CZTS types.

That the order-disorder transition occurs even in single-phase CZTS implies that the formation of an ordered state during cooling causes the phase splitting rather than vice versa. For some compositions reducing the presence of certain defects by ordering is what makes the formation of different defect complexes energetically favorable, instigating the phase splitting.

Further work investigating the reproducibility of the phase formation upon several cycles of heating and cooling would be enlightening, but was precluded during this study by the limited time available at Diamond. This would prove whether the phase convergence upon heating is simply a final homogenization of the sample, or whether the phase separation on cooling is truly energetically favorable, and would allow investigation into whether the exact same low-temperature state is always reached or whether the concentration of the respective defect complexes can be different.

5. Conclusions

Five samples of CZTS with a range of compositions were fabricated by solid state reaction. The secondary phases present in each were identified by EDX, ^{65}Cu NMR, and Raman spectroscopy. Their crystal structures were studied using high-resolution anomalous-scattering X-ray diffraction. All CZTS was found to adopt the kesterite crystal structure with significant cation disorder.

Three of the samples were found to contain two distinct kesterite CZTS phases with slightly different lattice parameters ($\Delta \sim 0.004 \text{ \AA}$) and different compositions. These are attributed to defect-complex-defined ‘types’ of CZTS, which have been previously reported.

All CZTS phases were found to belong to a specific type of CZTS, and two new types are proposed and explained. These are G-type, in which $[2\text{Cu}_{\text{Sn}^{3+}} + \text{Cu}_{\text{Zn}^{2+}} + \text{Cu}_{\text{I}^{+}} + 3\text{V}_{\text{S}^{2+}}]$ defects are prevalent, and H-type, in which $[3\text{S}_{\text{I}^{2+}} + \text{V}_{\text{Cu}^{+}} + \text{Zn}_{\text{Cu}^{+}} + 2\text{Sn}_{\text{Cu}^{3+}}]$ defects are prevalent. In both cases, the defects probably do not form a single complex due to their large number.

Above the order-disorder phase transition, at 600 K, the two CZTS phases converge to a single phase in two of the three samples. All samples exhibit more Cu-Zn disorder at 600 K than at 300 K, regardless of number of phase and their type.

A mechanism of phase formation in CZTS is thus proposed. Above the order-disorder transition a single phase of CZTS is generally formed, although in some cases two. In either case, the CZTS composition is defined by the overall energetic stability of the mixture of CZTS of that composition and any combination of secondary phases. As the sample cools below the order-disorder transition, the ordering of the CZTS phase may cause different defect complexes to become energetically favorable, and so the CZTS phase may split into two phases of different ‘types’. However, with the temperature too low to change the secondary phases present, these phases are confined by retaining an average composition of the initial CZTS phase. This mechanism clearly has important implications for designing the formation process of CZTS for solar photovoltaic applications.

This work was only possible because of the incredibly high resolution of the I11 beamline at Diamond, the highest resolution yet used to study the structure of CZTS. This is therefore the first time this two-phase structure has been observed using diffraction. Further work investigating the reproducibility of the phase formation upon several cycles of heating and cooling would be enlightening, as would a theoretical study of the formation energy and energetic stability not just of individual point defect complexes, but of a multi-phase sample as a function of phases present, phase fractions, and defect complex density within the CZTS phase(s). This more complex, overall stability is the real driver of phase formation and disorder in CZTS, and therefore of critical importance in increasing the photovoltaic efficiency of CZTS solar cells.

SUPPORTING INFORMATION

CIF files describing the refined structures of the CZTS phases in each sample at both 300 K and 600 K.

AUTHOR INFORMATION

Corresponding Author

* d.p.halliday@durham.ac.uk

ACKNOWLEDGMENT

This work was financially supported by the UK Engineering and Physical Sciences Research Council (award number 1335920), Diamond Light Source, and the University of Durham. Diamond Light Source supported this work with time on beamlines I11 and I15 under experiment numbers EE12564 and EE15370. Work at Diamond would not have been possible without the excellent technical staff and instrument scientists there. ICPMS measurements were kindly carried out by Dr Chris Ottley and NMR measurements by Dr David Apperley. Raman facilities were provided by Prof Andrew Beeby. Thanks also go to Jack Goodman, who assisted during some of the beamtime as part of an undergraduate project.

REFERENCES

- (1) *Global Market Outlook for Solar Power 2017-2021*. Solar Power Europe, 2017.
- (2) *Technology Roadmap for Solar Photovoltaic Energy 2014*. International Energy Agency, 2014.
- (3) Zuser, A.; Rechberger, H. Considerations of Resource Availability in Technology Development Strategies: The Case Study of Photovoltaics, *Resour., Conserv. Recycl.* **2011**, 56, 56-65, DOI: [10.1016/j.resconrec.2011.09.004](https://doi.org/10.1016/j.resconrec.2011.09.004)
- (4) Green, M. A.; Hishikawa, Y.; Warta, W.; Dunlop, E. D.; Levi, D. H.; Hohl-Ebinger, J.; Ho-Baillie, A. W. H. Solar Cell Efficiency Tables (Version 50), *Prog. Photovoltaics* **2017**, 25, 668-676, DOI: [10.1002/pip.2909](https://doi.org/10.1002/pip.2909)
- (5) Wang, W.; Winkler, M. T.; Gunawan, O.; Gokmen, T.; Todorov, T. K.; Zhu, Y.; Mitzi, D. B. Device Characteristics of CZTSSe Thin Film Solar Cells with 12.6% Efficiency, *Adv. Energy Mater.* **2013**, 4, 1301465.1-5, DOI: [10.1002/aenm.201301465](https://doi.org/10.1002/aenm.201301465)
- (6) Yoshikawa, K.; Kawasaki, H.; Yoshida, W.; Irie, T.; Konishi, K.; Nakano, K.; Uto, T.; Adachi, D.; Kanematsu, M.; Uzu, H.; Yamamoto, K. Silicon Heterojunction Solar Cell with Interdigitated Back Contacts for a Photoconversion Efficiency over 26%, *Nat. Energy* **2017**, 2, 17032.1-8, DOI: [10.1038/nenergy.2017.32](https://doi.org/10.1038/nenergy.2017.32)
- (7) Jackson, P.; Wuerz, R.; Hariskos, D.; Lotter, E.; Witte, W.; Powalla, M. Effects of Heavy Alkali Elements in Cu(In,Ga)Se₂ Solar Cells with Efficiencies up to 22.6%, *Phys. Status Solidi RRL* **2016**, 10, 583-586, DOI: [10.1002/pssr.201600199](https://doi.org/10.1002/pssr.201600199)
- (8) Liu, X.; Feng, Y.; Cui, H.; Liu, F.; Hao, X.; Conibeer, G.; Mitzi, D. B.; Green, M. The Current Status and Future Prospects of Kesterite Solar Cells: A Brief Review, *Prog. Photovoltaics* **2016**, 24, 879-898, DOI: [10.1002/pip.2741](https://doi.org/10.1002/pip.2741)
- (9) Gunawan, O.; Gokmen, T.; Mitzi, D. B. Suns-V_{oc} Characteristics of High-Performance Kesterite Solar Cells, *J. Appl. Phys.* **2014**, 116, 084504.1-9, DOI: [10.1063/1.4893315](https://doi.org/10.1063/1.4893315)
- (10) Scragg, J. J. S.; Larsen, J. K.; Kumar, M.; Persson, C.; Sendler, J.; Siebentritt, S.; Platzer Björkman, C. Cu-Zn Disorder and Band Gap Fluctuations in Cu₂ZnSn(S,Se)₄: Theoretical and Experimental Investigations, *Phys. Status Solidi B* **2016**, 253, 247-254, DOI: [10.1002/pssb.201552530](https://doi.org/10.1002/pssb.201552530)
- (11) Bosson, C. J.; Birch, M. T.; Halliday, D. P.; Knight, K. S.; Hatton, P. D. Cation Disorder and Phase Transitions in the Structurally Complex Solar Cell Material Cu₂ZnSnS₄, *J. Mater. Chem. A* **2017**, 5, 16672-16680, DOI: [10.1039/c7ta03603e](https://doi.org/10.1039/c7ta03603e)
- (12) Chen, S.; Gong, X. G.; Walsh, A.; Wei, S.-H. Crystal and Electronic Band Structure of Cu₂ZnSnX₄ (X=S and Se) Photovoltaic Absorbers: First-Principles Insights, *Appl. Phys. Lett.* **2009**, 94, 041903.1-3, DOI: [10.1063/1.3074499](https://doi.org/10.1063/1.3074499)
- (13) Maeda, T.; Nakamura, S.; Wada, T. Phase Stability and Electronic Structure of In-Free Photovoltaic Semiconductors, Cu₂ZnSnSe₄ and Cu₂ZnSnS₄ by First-Principles Calculation, *MRS Online Proc. Libr.* **2009**, 1165, 137-143, DOI: [10.1557/proc-1165-m04-03](https://doi.org/10.1557/proc-1165-m04-03)
- (14) Walsh, A.; Chen, S.; Wei, S.-H.; Gong, X.-G. Kesterite Thin Film Solar Cells: Advances in Materials Modelling of Cu₂ZnSnS₄, *Adv. Energy Mater.* **2012**, 2, 400-409, DOI: [10.1002/aenm.201100630](https://doi.org/10.1002/aenm.201100630)
- (15) Washio, T.; Nozaki, H.; Fukano, T.; Motohiro, T.; Jimbo, K.; Katagiri, H. Analysis of Lattice Site Occupancy in Kesterite Structure of Cu₂ZnSnS₄ Films Using Synchrotron Radiation X-ray Diffraction, *J. Appl. Phys.* **2011**, 110, 074511.1-4, DOI: [10.1063/1.3642993](https://doi.org/10.1063/1.3642993)
- (16) Schorr, S. The Crystal Structure of Kesterite Type Compounds: A Neutron and X-ray Diffraction Study, *Sol. Energy Mater. Sol. Cells* **2011**, 95, 1482-1488, DOI: [10.1016/j.solmat.2011.01.002](https://doi.org/10.1016/j.solmat.2011.01.002)
- (17) Espinosa-Faller, F. J.; Conradson, D. R.; Riha, S. C.; Martucci, M. B.; Fredrick, S. J.; Vogel, S.; Prieto, A. L.; Conradson, S. D. Neutron Diffraction and X-ray Absorption Fine Structure Evidence for Local Lattice Distortions and Aperiodic Antisite Substitution in Cu₂ZnSnS₄ Nanoparticles, *J. Phys. Chem. C* **2014**, 118, 26292-26303, DOI: [10.1021/jp502150s](https://doi.org/10.1021/jp502150s)
- (18) Lafond, A.; Choubrac, L.; Guillot-Deudon, C.; Fertey, P.; Evain, M.; Jobic, S. X-ray Resonant Single-Crystal Diffraction Technique, a Powerful Tool to Investigate the Kesterite Structure of the Photovoltaic Cu₂ZnSnS₄ Compound, *Acta Crystallogr., Sect. B: Struct. Sci., Cryst. Eng. Mater.* **2014**, 70, 390-394, DOI: [10.1107/s2052520614003138](https://doi.org/10.1107/s2052520614003138)
- (19) Ritscher, A.; Just, J.; Dolotko, O.; Schorr, S.; Lerch, M.; A Mechanochemical Route to Single Phase Cu₂ZnSnS₄ Powder, *J. Alloys Compd.* **2016**, 670, 289-296, DOI: [10.1016/j.jallcom.2016.02.058](https://doi.org/10.1016/j.jallcom.2016.02.058)
- (20) Chen, S.; Yang, J.-H.; Gong, X. G.; Walsh, A.; Wei, S.-H. Intrinsic Point Defects and Complexes in the Quaternary Kesterite Semiconductor Cu₂ZnSnS₄, *Phys. Rev. B* **2010**, 81, 245204.1-10, DOI: [10.1103/physrevb.81.245204](https://doi.org/10.1103/physrevb.81.245204)
- (21) Nagoya, A.; Asahi, R.; Wahl, R.; Kresse, G.; Defect Formation and Phase Stability of Cu₂ZnSnS₄ Photovoltaic Material, *Phys. Rev. B* **2010**, 81, 113202.1-4, DOI: [10.1103/physrevb.81.113202](https://doi.org/10.1103/physrevb.81.113202)
- (22) Malerba, C.; Azanza Ricardo, C. L.; Valentini, M.; Biccari, F.; Müller, M.; Rebuffi, L.; Esposito, E.; Mangiapane, P.; Scardi, P.; Mittiga, A. Stoichiometry Effect on Cu₂ZnSnS₄ Thin Films Morphological and Optical Properties, *J. Renewable Sustainable Energy* **2014**, 6, 011404.1-12, DOI: [10.1063/1.4866258](https://doi.org/10.1063/1.4866258)
- (23) Choubrac, L.; Lafond, A.; Guillot-Deudon, C.; Moëlo, Y.; Jobic, S. Structure Flexibility of the Cu₂ZnSnS₄ Absorber in Low-Cost Photovoltaic Cells: From the Stoichiometric to the Copper-Poor Compounds, *Inorg. Chem.* **2012**, 51, 3346-3348, DOI: [10.1021/ic202569q](https://doi.org/10.1021/ic202569q)
- (24) Chen, S.; Walsh, A.; Gong, X.-G.; Wei, S.-H.; Classification of Lattice Defects in the Kesterite Cu₂ZnSnS₄ and Cu₂ZnSnSe₄ Earth-Abundant Solar Cell Absorbers, *Adv. Mater.* **2013**, 25, 1522-1539, DOI: [10.1002/adma.201203146](https://doi.org/10.1002/adma.201203146)
- (25) Chen, S.; Gong, X. G.; Walsh, A.; Wei, S.-H.; Defect Physics of the Kesterite Thin Film Solar Cell Absorber Cu₂ZnSnS₄, *Appl. Phys. Lett.* **2010**, 96, 021902.1-3, DOI: [10.1063/1.3275796](https://doi.org/10.1063/1.3275796)
- (26) Lafond, A.; Choubrac, L.; Guillot-Deudon, C.; Deniard, P.; Jobic, S. Crystal Structures of Photovoltaic Chalcogenides, an Intricate Puzzle to Solve: The Cases of CIGSe and CZTS Materials, *Z. Anorg. Allg. Chem.* **2012**, 638, 2571-2577, DOI: [10.1002/zaac.201200279](https://doi.org/10.1002/zaac.201200279)
- (27) Gurieva, G.; Dimitrievska, M.; Zander, S.; Pérez-Rodríguez, A.; Izquierdo-Roca, V.; Schorr, S. Structural Characterization of Cu_{2.04}Zn_{0.91}Sn_{1.05}S_{2.08}Se_{1.92}, *Phys. Status Solidi C* **2015**, 12, 588-591, DOI: [10.1002/pssc.201400307](https://doi.org/10.1002/pssc.201400307)
- (28) Valle-Rios, L. E.; Neldner, K.; Gurieva, G.; Schorr, S. Existence of Off-Stoichiometric Single Phase Kesterite, *J. Alloys Compd.* **2016**, 657, 408-413, DOI: [10.1016/j.jallcom.2015.09.198](https://doi.org/10.1016/j.jallcom.2015.09.198)
- (29) Ritscher, A.; Franz, A.; Schorr, S.; Lerch, M. Off-stoichiometric CZTS: Neutron Scattering Investigations on Mechanochemically Synthesized Powders, *J. Alloys Compd.* **2016**, 689, 271-277, DOI: [10.1016/j.jallcom.2016.07.298](https://doi.org/10.1016/j.jallcom.2016.07.298)
- (30) Schorr, S.; Gonzalez-Aviles, G. In-Situ Investigation of the Structural Phase Transition in Kesterite, *Phys. Status Solidi A* **2009**, 206, 1054-1058, DOI: [10.1002/pssa.200881214](https://doi.org/10.1002/pssa.200881214)
- (31) Scragg, J. J. S.; Choubrac, L.; Lafond, A.; Ericson, T.; Platzer-Björkman, C. A Low-Temperature Order-Disorder Transition in Cu₂ZnSnS₄ Thin Films, *Appl. Phys. Lett.* **2014**, 104, 041911.1-4, DOI: [10.1063/1.4863685](https://doi.org/10.1063/1.4863685)
- (32) Ritscher, A.; Hoelzel, M.; Lerch, M. The Order-Disorder Transition in Cu₂ZnSnS₄ - A Neutron Scattering Investigation, *J. Solid State Chem.* **2016**, 238, 68-73, DOI: [10.1016/j.jssc.2016.03.013](https://doi.org/10.1016/j.jssc.2016.03.013)

- (33) Olekseyuk, I. D.; Dudchak, I. V.; Piskach, L. V. Phase Equilibria in the $\text{Cu}_2\text{S-ZnS-SnS}_2$ System, *J. Alloys Compd.* **2004**, *368*, 135-143, DOI: [10.1016/j.jallcom.2003.08.084](https://doi.org/10.1016/j.jallcom.2003.08.084)
- (34) Scragg, J. *PhD thesis*, University of Bath, 2010.
- (35) Kumar, M.; Dubey, A.; Adhikari, N.; Venkatesan, S.; Qiao, Q. Strategic Review of Secondary Phases, Defects and Defect-Complexes in Kesterite CZTS-Se Solar Cells, *Energy Environ. Sci.* **2015**, *8*, 3134-3159, DOI: [10.1039/c5ee02153g](https://doi.org/10.1039/c5ee02153g)
- (36) Berg, D. M.; Arasimowicz, M.; Djemour, R.; Gütay, L.; Siebentritt, S.; Schorr, S.; Fontané, X.; Izquierdo-Roca, V.; Pérez-Rodríguez, A.; Dale, P. J. Discrimination and Detection Limits of Secondary Phases in $\text{Cu}_2\text{ZnSnS}_4$ Using X-ray Diffraction and Raman Spectroscopy, *Thin Solid Films* **2014**, *569*, 113-123, DOI: [10.1016/j.tsf.2014.08.028](https://doi.org/10.1016/j.tsf.2014.08.028)
- (37) Thompson, S. P.; Parker, J. E.; Potter, J.; Hill, T. P.; Birt, A.; Cobb, T. M.; Yuan, F.; Tang, C. C. Beamline I11 at Diamond: A New Instrument for High Resolution Powder Diffraction, *Rev. Sci. Instrum.* **2009**, *80*, 075107.1-9, DOI: [10.1063/1.3167217](https://doi.org/10.1063/1.3167217)
- (38) Choubrac, L.; Paris, M.; Lafond, A.; Guillot-Deudon, C.; Rocquefelte, X.; Jobic, S.; Multinuclear (^{67}Zn , ^{119}Sn and ^{65}Cu) NMR Spectroscopy - An Ideal Technique to Probe the Cationic Ordering in $\text{Cu}_2\text{ZnSnS}_4$ Photovoltaic Materials, *Phys. Chem. Chem. Phys.* **2013**, *15*, 10722-10725, DOI: [10.1039/c3cp51320c](https://doi.org/10.1039/c3cp51320c)
- (39) Gürel, T.; Sevik, C.; Çağın, T. Characterization of Vibrational and Mechanical Properties of Quaternary Compounds $\text{Cu}_2\text{ZnSnS}_4$ and $\text{Cu}_2\text{ZnSnSe}_4$ in Kesterite and Stannite Structures, *Phys. Rev. B* **2011**, *84*, 205201.1-7, DOI: [10.1103/physrevb.84.205201](https://doi.org/10.1103/physrevb.84.205201)
- (40) Khare, A.; Himmertoglu, B.; Johnson, M.; Norris, D. J.; Cococcioni, M.; Aydil, E. S. Calculation of the Lattice Dynamics and Raman Spectra of Copper Zinc Tin Chalcogenides and Comparison to Experiments, *J. Appl. Phys.* **2012**, *111*, 083707.1-9, DOI: [10.1063/1.4704191](https://doi.org/10.1063/1.4704191)
- (41) Dumcenco, D.; Huang, Y.-S. The Vibrational Properties Study of Kesterite $\text{Cu}_2\text{ZnSnS}_4$ Single Crystals by Using Polarization Dependent Raman Spectroscopy, *Opt. Mater.* **2013**, *35*, 419-425, DOI: [10.1016/j.optmat.2012.09.031](https://doi.org/10.1016/j.optmat.2012.09.031)
- (42) Dimitrievska, M.; Fairbrother, A.; Pérez-Rodríguez, A.; Saucedo, E.; Izquierdo-Roca, V. Raman Scattering Crystalline Assessment of Polycrystalline $\text{Cu}_2\text{ZnSnS}_4$ Thin Films for Sustainable Photovoltaic Technologies: Phonon Confinement Model, *Acta Mater.* **2014**, *70*, 272-280, DOI: [10.1016/j.actamat.2014.02.035](https://doi.org/10.1016/j.actamat.2014.02.035)
- (43) Cheng, Y. C.; Jin, C. Q.; Gao, F.; Wu, X. L.; Zhong, W.; Li, S. H.; Chu, P. K.; Raman Scattering Study of Zinc Blende and Wurtzite ZnS , *J. Appl. Phys.* **2009**, *106*, 123505.1-5, DOI: [10.1063/1.3270401](https://doi.org/10.1063/1.3270401)
- (44) Munce, C. G.; Parker, G. K.; Holt, S. A.; Hope, G. A.; A Raman Spectroelectrochemical Investigation of Chemical Bath Deposited Cu_xS Thin Films and Their Modification, *Colloids Surf. A* **2007**, *295*, 152-158, DOI: [10.1016/j.colsurfa.2006.08.045](https://doi.org/10.1016/j.colsurfa.2006.08.045)
- (45) Fernandes, P. A.; Salomé, P. M. P.; da Cunha, A. F. Study of Polycrystalline $\text{Cu}_2\text{ZnSnS}_4$ Films by Raman Scattering, *J. Alloys Compd.* **2011**, *509*, 7600-7606, DOI: [10.1016/j.jallcom.2011.04.097](https://doi.org/10.1016/j.jallcom.2011.04.097)

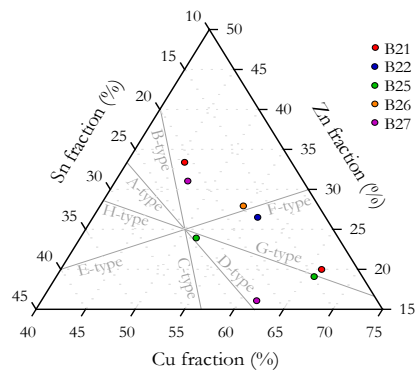


Table of Contents artwork
